Quantifying the impact of charge rate and number of cycles on structural degeneration of Li-ion battery electrodes

Orkun Furat[1,*], Donal P. Finegan[2,*], Zhenzhen Yang[3], Tanvir R. Tanim[4], Kandler Smith[2], Volker Schmidt[1]

[1] *Institute of Stochastics, Ulm University, Helmholtzstraße 18, 89069 Ulm, Germany*
[2] *National Renewable Energy Laboratory, 15013 Denver W Parkway, Golden, CO 80401, USA*
[3] *Chemical Sciences and Engineering Division, Argonne National Laboratory, 9700 S. Cass Avenue, Lemont, IL 60439, USA*
[4] *Idaho National Laboratory, 2525 N. Fremont, Idaho Falls, ID 83415, USA*

Abstract

A quantitative link between crack evolution in lithium-ion positive electrodes and the degrading performance on cells is not yet well established nor is any single technique capable of doing so widely available. Here, we demonstrate a widely accessible high-throughput approach to quantifying crack evolution within electrodes. The approach applies super-resolution scanning electron microscopy (SEM) imaging of cross-sectioned NMC532 electrodes, followed by segmentation and quantification of crack features. Crack properties such as crack intensity, crack width and length are quantified as a function of charge rate (1C, 6C, and 9C) and cycle number (25, 225, and 600 cycles). Hundreds of particles are characterized for statistical confidence in the quantitative crack measurements. The data on crack evolution is compared to electrochemical data from full cells and half cells with the NMC532 positive electrodes. We show that while crack evolution strongly correlates with capacity fade in the first 25 cycles, it does not correlate well for the following hundreds of cycles indicating that cracking may not be the dominant cause of capacity fade throughout the cycle-life of cells.

Keywords:—Lithium-ion battery, cathode particle, aging, crack evolution, statistical image analysis, super-resolution.

1 Introduction

Lithium (Li) ion batteries are now widespread and continue to rapidly increase in deployment for use in electric vehicles and grid-scale storage. Most commercial high energy density cells of around $250\,\mathrm{Wh\,kg^{-1}}$ already achieve up to 1000 cycles before they reach the end of their cycle life or 80 % of their original capacity. Extending the cycle-life of cells beyond the state-of-the-art today would have tremendous economic impact including long-life electric vehicles and grid-scale storage solutions. The cycle life of a cell is dictated by its rate of capacity degradation, the cause of which is a complex mix of unfavorable mechanical, chemical, and electrochemical phenomena within the cell. Building an understanding of dominant degradation mechanisms is critical for designing future iterations of Li-ion cells with enhanced cycle lives.

For positive electrodes consisting of $\mathrm{LiNi}_x\mathrm{Mn}_y\mathrm{Co}_z\mathrm{O}_2$ (NMC), one of the dominant modes of degradation is widely considered to be mechanical degradation in the form of cracking of individual NMC particles. To date, almost all commercial NMC electrodes consist of polycrystalline particle architectures[1] and it has been widely observed that such polycrystalline particles crack throughout the cycle life of cells.[2–4] The cause of particle cracking is likely due to sub-particle mechanical strain causing nucleation and propagation of cracks throughout the electrode's cycle life. Sub-particle strain arises from the anisotropic expansion and contraction of NMC crystallites during lithiation and

*Corresponding authors
Email addresses: orkun.furat@uni-ulm.de (Orkun Furat), donal.finegan@nrel.gov (Donal P. Finegan)

delithiation. Compositional and crystallographic variations throughout particles can also exacerbate this internal strain and accelerate cracking due to undergoing crystallographic phase changes within their operating voltage range.[5–7] In an effort to model a representative particle, a series of recent papers outline a method to characterize[1,8] and artificially generate representative digital twins of single NMC particle architectures[9] that were then used in a 3D multi-physics model[10] to show how particle fracture occurs. The model showed sub-particle strain maps that arise from non-ideal grain interactions during their respective anisotropic morphology changes throughout operation. Other modeling efforts came to similar conclusions[11–13] and recent work has shown that modifying the orientation and morphology of grains to be more favorable (e.g. radially aligned grains) which can mitigate mechanical damage within particles and extend the cycle-life of cells.[14,15]

Despite numerous observations that cracks become worse throughout the cycle life of NMC electrodes, the particle porosity has never been quantified as a function of cycle history and therefore the direct link between cracks and capacity fade remains unfulfilled. Quantifying crack growth by means of image data is extremely challenging due to the need for both high spatial resolution to resolve cracks and the large field of view to achieve statistical significance of the data. X-ray nano-computed tomography has been demonstrated as a successful technique for measuring cracks throughout numerous particles[16,17] and may be applied to provide statistically significant data on crack evolution. Segmentation methods that apply machine learning have demonstrated that crack quantification in CT images can be automated with a high degree of accuracy.[18] However, nano-CT is currently limited to a few synchrotron facilities or high-end lab equipment and is therefore not widely accessible. Finding a technique that facilitates accessible and high-throughput quantification for dynamic feedback for manufactures looking for solutions to cracking is essential to accelerate the evolution of long-life electrodes.

Scanning electron microscopy (SEM) is a widely accessible technique and can facilitate high-throughput imaging with rapid feedback to materials scientists. To address the challenge of high-resolution imaging for resolving cracks having small fields of view that do not achieve good statistics, a super-resolution technique was recently demonstrated to enhance the resolution of large field of view (FOV) images for crack quantification.[19] More precisely, a so-called SRGAN[20] architecture has been trained with pairs of low- and high-resolution SEM images depicting cycled cathode particles to artificially enhance the resolution of low-resolution SEM images. This method has been quantitatively validated, indicating that super-resolution techniques allows for a better quantification of fine features such as cracks.

Here, we enhance the resolution of 93 large FOV SEM images taken from cross-sectioned NMC532 electrodes that were cycled under different rates of charge to difference cycle numbers. For that purpose, we deploy the trained SRGAN network considered in Furat et al. (2022)[19] to obtain super-resolved versions of the SEM image data. Then, we segment and quantify the evolution of cracks with respect to their prevalence, width, and length as a function of cycle number (25, 225, 600) and of charge rate (1C, 6C, and 9C). Correlations between crack evolution and the electrochemical response of the positive electrodes are made. It is expected that demonstration of this approach will accelerate the use of high-throughput crack quantification via SEM images, clarify the correlation between crack growth and cell performance, and facilitate rapid validation of crack-mitigation measures using novel synthesis approaches.

2 Methods

2.1 Sample details and preparation

The NMC cathode and Gr anodes were fabricated at Argonne National Laboratory's (Argonne's) Cell Analysis, Modeling, and Prototyping (CAMP) facility. The cathode was made from NMC532 (Toda, 90 wt%) with 5 wt% PVDF and 5 wt% C45 carbon black. The coating thickness is 42 µm with 34.1 % porosity. Detailed cell build parameters for the single layer pouch cells can be found in our previous publication.[21]

A subset of cells at different cycling intervals was intermittently removed from cycling and disassembled in an Ar-filled glovebox. Cross-sectional scanning electron microscopy was used to characterize the evolution of cracks in NMC532 cathodes after different charging rates and cycle counts. The cross-sectional electrode samples were obtained using Ar+ ion milling and imaged using JEOL JSM-6610LV SEM instrument in the backscattering mode The detailed parameter for cross-polisher and SEM can be found in ref.[21].

Altogether, we obtained 9 scanning electron microscopy (SEM) images of pristine cathodes and several (about

nine) SEM images for each of the 9 degradation scenarios (i, j) with $i \in \{1\text{C}, 6\text{C}, 9\text{C}\}, j \in \{25, 225, 600\}$ of cathodes considered in the present paper.

2.2 Acquisition of electrochemical data

Thirty single layer pouch cells (xx3450 format) were built by Cell Analysis, Modeling, and Prototyping (CAMP) Facility at Argonne National Laboratory (Argonne) and tested at Idaho National Laboratory (INL). Cycling was performed in a thermally controlled chamber (TestEquity 1007C) at 30 °C using the Maccor 4000 series automated-test system. The post-formation capacity tests at C/20 and C/1 resulted 20 mAh and 19.7 mAh with less than 1 % 1σ variability. The cells were then divided into separate groups for cycle life evaluation at different charging rates (11 cells at 1C, 8 cells at 6C and 11 cells at 9C) between 3 to 4.1 V. After each charge, the cells were relaxed for 15 min, which followed by a C/2 discharge to 3 V. Another 15 min rest was added before the next charge step. Cycling was paused at different cycling intervals to perform the reference performance test (RPT) that included C/20 capacity and electrochemical impedance spectroscopy tests. A subset of cells was taken off test at 25, 225, and 600 cycles for tear down post-testing and additional characterizations including SEM. From each single layer pouch cell cathode, three 1.27 cm diameter electrodes were used to build coin cells against 1.43 cm-diameter, 170 µm-thick Li reference electrode with the same separator and fresh electrolyte. After formation, cathode capacity was measured using a slow rate (C/20) discharge capacity between 2.8 to 4.3 V. This C/20 discharge capacity at different cycling intervals was used to determine loss of active material (LAM) in the cathode upon comparing similar data from the uncycled sample's coin cell. More detail about cell build and testing procedure can be found in Tanim et al. (2021).[21]

2.3 Data preprocessing

For a quantitative analysis of crack formation in $\text{LiNi}_{1-x-y}\text{Mn}_y\text{Co}_x\text{O}_2$ (NMC) particles of differently aged cathodes, the SEM images $I\colon W = \{1, \dots, w\} \times \{1, \dots, h\} \to [0, 1]$ with width $w = 2560$ and height $h = 1920$, the acquisition of which has been described in Section 2.1, have to be segmented. Therefore, we distinguish between the phase-wise and crack-wise segmentation of image data, where the former is a map which associates each pixel with either the background, a particle or a crack. More precisely, a phase-wise segmentation of I is an image $S\colon W \to \{0, 1, 2\}$ with

$$S(x) = \begin{cases} 1, & \text{if } x \text{ corresponds to a particle,} \\ 2, & \text{if } x \text{ corresponds to a crack,} \\ 0, & \text{else,} \end{cases} \tag{1}$$

for each $x \in W$. Furthermore, a crack-wise segmentation is a partition of the crack phase $C = \{x \in W : S(x) = 2\}$, which allows for the extraction of individual cracks from image data for their quantitative analysis. In other words, a crack-wise segmentation of I into $n > 0$ cracks is a map $S_\text{c}\colon W \to \{0, \dots, n\}$ with

$$S_\text{c}(x) = \begin{cases} i, & \text{if } x \text{ belongs to the } i\text{-th crack,} \\ 0, & \text{else,} \end{cases} \tag{2}$$

such that $C = \{x \in W\colon S_\text{c}(x) > 0\}$.

2.3.1 Super-resolution

It has been shown in Furat et al. (2022)[19] that segmentation results for fine features such as cracks can be improved by super-resolving the (raw, i.e. low-resolution) SEM image I prior to segmentation. In particular, in Furat et al. (2022)[19] a generative adversarial network (GAN), denoted by SRGAN, has been trained with pairs of the low-resolution SEM image data and corresponding high-resolution versions to artificially increase the resolution of the low-resolution images by a factor of 2.5. Therefore, we use the trained SRGAN to super-resolve the raw SEM images I to obtain high-resolution versions $I_\text{SR}\colon W' \to [0, 1]$, where $W' = \{1, \dots, 2.5w\} \times \{1, \dots, 2.5h\} = \{1, \dots, 6400\} \times \{1, \dots, 4800\}$, see Figure 1.

For keeping the notation possibly simple, we also denote super-resolved images by $I\colon W \to [0, 1]$ from here on.

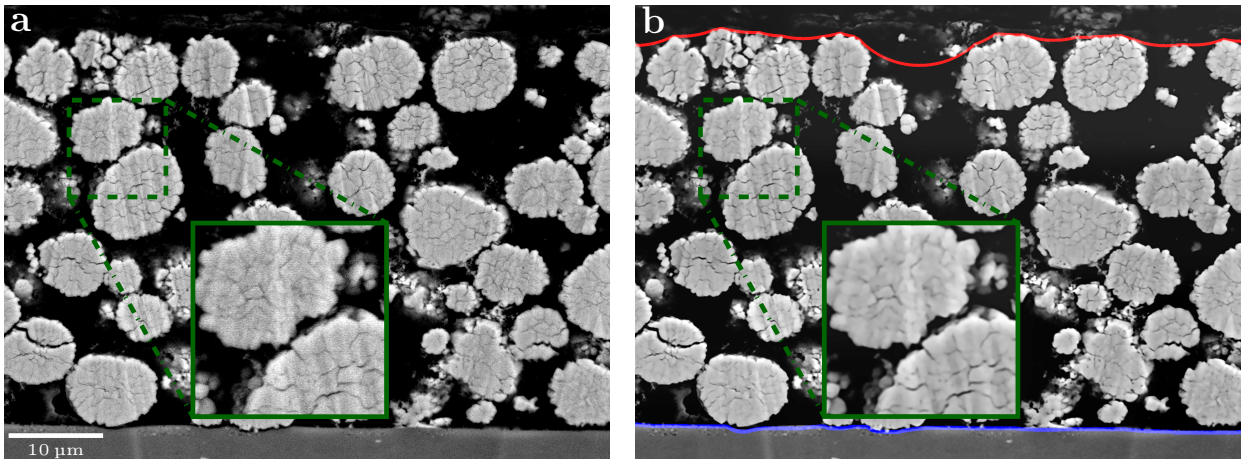

Figure 1: **Super-resolution.** Raw SEM image I (a) and the super-resolved version I_{SR} (b) computed by the trained SRGAN network. Magnifications with a zoom factor of 2 of the dashed green squares are visualized in the green solid-lined squares. Pixels associated with the cathode and separator surface are visualized in red and blue, respectively. All figures use the same length scale.

2.3.2 Phase-wise segmentation

In order to compute a phase-wise segmentation S of a super-resolved image I we deploy a convolutional neural network (CNN), namely a modified U-Net[22] denoted by UNET. More precisely, we use a tensorflow[23] implementation of a U-Net with a U-depth[24] of 5 for which the number f_0 of filters in the first convolutional layer is set equal to 32. Furthermore, we set the padding of all convolutional layers to SAME and the dilation rate of all hidden convolutional layers equal to 4. The output layer has three channels and the softmax function as activation function. Thus, for an input image $I\colon W \to [0,1]$ the output $\widehat{Y} = \mathrm{UNET}(I)$ is a map $\widehat{Y}\colon W \times \{1,2,3\} \to [0,1]$ with $\widehat{Y}(x,1) + \widehat{Y}(x,2) + \widehat{Y}(x,3) = 1$, i.e., the values $\widehat{Y}(x,1), \widehat{Y}(x,2), \widehat{Y}(x,3)$ can be considered to be probabilities with which a pixel $x \in W$ is associated with the background, a particle or a crack, respectively.

In order to train the network, we manually annotated $n = 8$ super-resolved images, i.e., we have grayscale images $I^{(1)}, \ldots, I^{(n)}\colon W \to [0,1]$ with corresponding segmentation maps $S^{(1)}, \ldots, S^{(n)}\colon W \to \{0,1,2\}$. For training purposes, we transform the segmentation maps $S^{(i)}$ to one-hot-encoded versions $Y^{(i)}\colon W \times \{1,2,3\} \to \{0,1\}$ given by

$$Y^{(i)}(x,c) = \begin{cases} 1, & \text{if } S^{(i)}(x) = c, \\ 0, & \text{else}, \end{cases} \tag{3}$$

for each $(x,c) \in W \times \{1,2,3\}$ and $i = 1, \ldots, n$. The discrepancy between an annotated one-hot-encoded image $Y^{(i)}$ and the network's output $\widehat{Y}^{(i)} = \mathrm{UNET}(I^{(i)})$ for an input image $I^{(i)}$ is quantified by the weighted categorical cross entropy CE as a loss function which is given by

$$\mathrm{CE}(\widehat{Y}^{(i)}, Y^{(i)}) = -\sum_{x \in W} \sum_{c=1}^{3} w_c \, Y^{(i)}(x,c) \log\Big(\widehat{Y}^{(i)}(x,c)\Big), \tag{4}$$

where the weight vector $w = (w_1, w_2, w_3)$ is set to $(0.248, 0.232, 0.52)$ in order to handle class imbalance.[25,26] Training a network entails minimizing such discrepancies by adapting the network's parameters which are also referred to as trainable weights. This is achieved by using the stochastic gradient descent algorithm Adam[27] with a learning rate of 10^{-4} and a batchsize of 1. The batches are generated during training by randomly taking cutouts from the pairs $I^{(i)}, Y^{(i)}$ for $i = 1, \ldots, n-1$, whereas $I^{(n)}, Y^{(n)}$ will be used for validation purposes. More precisely, during training, a data augmentation procedure[28] takes (randomly rotated) cutouts $I^{\mathrm{cut}}\colon W^{\mathrm{cut}} \to [0,1]$, $Y^{\mathrm{cut}}\colon W^{\mathrm{cut}} \times \{1,2,3\} \to \{0,1\}$ from the training data $I^{(i)}, Y^{(i)}$ for $i = 1, \ldots, n-1$, respectively, where the square sampling window $W^{\mathrm{cut}} \subset W$ has a side length of 1024. Furthermore, the data augmentation procedure adds Gaussian white noise with standard deviation of 0.1 to the pixel values of the cutouts I^{cut}.

In order to terminate training, we use an early stopping criterion.[27] Therefore, prior to training, using the data augmentation procedure described above, 50 pairs of cutouts are taken from $I^{(n)}, Y^{(n)}$. After every 200 training steps, a validation step is performed by evaluating the network's performance with respect to these 50 pairs of cutouts. The training procedure is terminated if the performance of the network does not improve within 10 such validation steps. Then, the network's trainable weights are set to the values for which the network had performed best at a validation step.

After training, the network can be applied to the entire SEM image data of aged cathodes, i.e., for each super-resolved SEM image I we compute $\widehat{Y} = \mathrm{UNET}(I)$, see Figure 2 (center block). Note that, since the values of $\widehat{Y}$ correspond to probabilities, the map $\widehat{Y}$ cannot be considered to be segmentation as defined in Equation (1) yet. Therefore, using an additional processing step, we compute a phase-wise segmentation map $S\colon W \to \{0,1,2\}$ from the network output $\widehat{Y}$ by

$$S(x) = \begin{cases} 2, & \text{if } \widehat{Y}(x,3) \geq t, \\ 1, & \text{if } \widehat{Y}(x,3) < t \text{ and } \widehat{Y}(x,2) \geq \widehat{Y}(x,1), \\ 0, & \text{else,} \end{cases} \tag{5}$$

for each $x \in W$, where the threshold $t > 0$ is chosen manually. The final segmentation result is visualized in Figure 2 (right block).

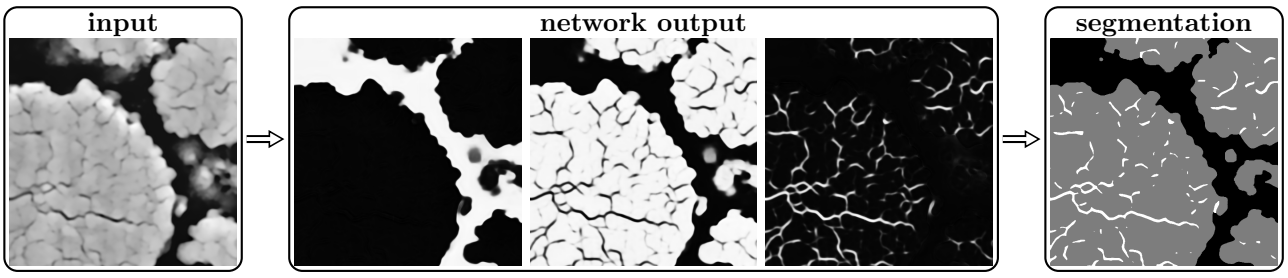

Figure 2: **Phase-wise segmentation procedure.** The trained U-Net processes input SEM images I (left block) into probability maps $\widehat{Y}$ (center block) for the background $\widehat{Y}(\cdot,1)$ (center block, left), the particles $\widehat{Y}(\cdot,2)$ (center block, middle) and the cracks $\widehat{Y}(\cdot,3)$ (center block, right), where black color corresponds to a probability of 0 and white to a probability of 1. Using the post-processing step given by Equation (5) we obtain the final phase-wise segmentation S of I (right block).

2.3.3 Crack-wise segmentation

To quantitatively analyze individual cracks, the phase-wise segmentation S determined by means of Equation (5) has to be further segmented into individual cracks. Therefore, we skeletonize the crack phase $C = \{x \in W : S(x) = 2\}$ of S using the method described in Lee et al. (1994).[29] This results in a binary skeleton image $C_{\mathrm{skelet}}\colon W \to \{0,1\}$, where the crack phase is represented by a network of $n_{\mathrm{skelet}} > 0$ discretized curves $L_1, \ldots, L_{n_{\mathrm{skelet}}} \subset W$, see Figure 3 (center block). We consider each curve L_i to be representative for an individual crack. By assigning each pixel associated with the crack phase to the closest curve L_i we obtain a crack-wise segmentation $S_{\mathrm{c}}\colon W \to \{0, \ldots, n_{\mathrm{skelet}}\}$ of I. More precisely, the crack-wise segmentation S_{c} is given by

$$S_{\mathrm{c}}(x) = \begin{cases} i, & \text{if } x \in C,\ \mathrm{dist}(x,L_i) < \mathrm{dist}(x,L_j) \text{ for each } j = 1,\ldots,i-1, \\ & \quad \text{and } \mathrm{dist}(x,L_i) \leq \mathrm{dist}(x,L_j) \text{ for each } j = i+1,\ldots,n_{\mathrm{skelet}}, \\ 0, & \text{else,} \end{cases} \tag{6}$$

for each $x \in W$, where $\mathrm{dist}(x,L_i)$ denotes the Euclidean distance of $x \in C$ to the discretized curve L_i, i.e.,

$$\mathrm{dist}(x,L_i) = \min_{y \in L_i} \|x - y\|, \tag{7}$$

with $\|\cdot\|$ denoting the Euclidean norm in $\mathbb{R}^2$, see Figure 3 (right block). Thus, if two curves L_i and L_j with $i < j$ are closest to some pixel $x \in C$ with $\mathrm{dist}(x,L_i) = \mathrm{dist}(x,L_j)$, we set the value of $S_{\mathrm{c}}(x)$ to i. From the crack-wise

segmentation S_c individual cracks $s_i \subset W$ can be extracted, where

$$s_i = \{x \in W \colon S_c(x) = i\} \qquad \text{for each } i = 1, \ldots, n_{\text{skelet}}. \tag{8}$$

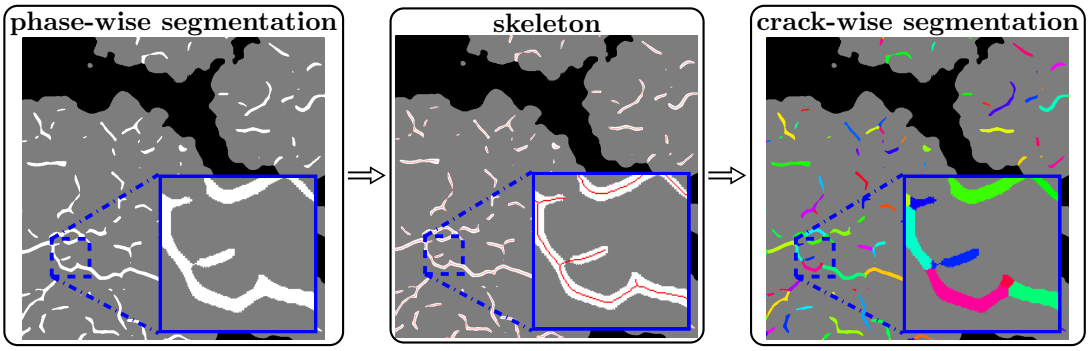

Figure 3: **Crack-wise segmentation procedure.** The background, particle and crack phases of the phase-wise segmentation S (left block) are visualized in black, gray and white, respectively. In a first step, the skeleton C_{skelet} (center block, red curves) of the phase-wise segmentation S is computed. Then, in a second step, the crack phase is segmented by associating each pixel of the crack phase with the closest curve in the skeleton. Each crack of the resulting crack-wise segmentation S_c (right block) is colored individually. Magnifications with a zoom factor 4 of the dashed blue squares are visualized in the blue solid-lined squares.

2.4 Cathode and crack descriptors

Using both the phase-wise and crack-wise segmentations S and S_c of a super-resolved SEM image I we can compute descriptors for quantifying and characterizing the cathode thickness, the particle porosity as well as the intensity, size and shape of individual cracks. Such structural descriptors of degraded cathodes can then be correlated with battery cycling parameters, in order to investigate the influence of the C-rate or the number of cycles on the structural degradation. In this section we describe the procedure which we used for the computation of structural descriptors for the case of pristine cathodes. For degraded cathodes, i.e., for the degradation scenarios (i, j) with $i \in \{1\text{C}, 6\text{C}, 9\text{C}\}, j \in \{25, 225, 600\}$ this procedure can be performed analogously.

2.4.1 Cathode thickness

Let $I^{(1)}, \ldots, I^{(m)}$ denote the $m = 9$ SEM images of pristine cathodes with the corresponding phase-wise segmentations $S^{(1)}, \ldots, S^{(m)}$ and crack-wise segmentations $S_c^{(1)}, \ldots, S_c^{(m)}$. In order to determine the local cathode thickness, i.e., the vertical distances of the separator to the cathode surface for each x-coordinate $x = 1, \ldots, 6400$, the cathode surface has to be identified. For that purpose we deploy the so-called rolling ball approach onto the phase-wise segmentations $S^{(1)}, \ldots, S^{(m)}$.[30,31] More precisely, in this approach a disk with a relatively large radius of 8.75 µm rolled along the cathode surface—all pixels which cannot be reached by the disk are considered to be associated with the cathode, thus, defining the surface of the cathode, see Figure 1b (red line). For each $i = 1, \ldots, m$, the cathode surface in $I^{(i)}$ can be considered as a function $\text{surf}_{\text{cathode}}^{(i)} \colon \{1, \ldots, 6400\} \to \{1, \ldots, 4800\}$, where the value $\text{surf}_{\text{cathode}}^{(i)}(x)$ is the height of the cathode's surface at the x-coordinate $x \in \{1, \ldots, 6400\}$. On the other hand, the surface of the separator is determined manually, resulting in a functions $\text{surf}_{\text{separator}}^{(i)} \colon \{1, \ldots, 6400\} \to \{1, \ldots, 4800\}$ for each $i = 1, \ldots, m$, see Figure 1b (blue line). Then, the local thickness $t^{(i)} \colon \{1, \ldots, 6400\} \to [0, \infty)$ of the cathode depicted in $I^{(i)}$ is given by

$$t^{(i)}(x) = p \, |\text{surf}_{\text{cathode}}^{(i)}(x) - \text{surf}_{\text{separator}}^{(i)}(x)|, \tag{9}$$

for each x-coordinate $x \in \{1, \ldots, 6400\}$ and $i = 1, \ldots, m$, where $p = 0.01$ µm denotes the pixel size. Thus, we obtain the dataset $T_{\text{pristine}} = (t(x)^{(i)})_{x=1,i=1}^{6400,9}$ of local thickness values for pristine cathodes.

2.4.2 Particle porosity

The overall amount of cracks can be characterized by the particle porosity $\rho \in [0,1]$ which is given by the area fraction of the crack phases in $S^{(1)}, \ldots, S^{(m)}$ with respect to the union of the particle and crack phases in $S^{(1)}, \ldots, S^{(m)}$, i.e.,

$$\rho = \frac{\sum_{i=1}^{m} \#\{x \in W \colon S^{(i)}(x) = 2\}}{\sum_{i=1}^{m} \#\{x \in W \colon S^{(i)}(x) > 0\}}, \tag{10}$$

where # denotes the cardinality of the set under consideration.

2.4.3 Intensity, size and shape of individual cracks

Additionally, we consider the intensity $\lambda > 0$ of cracks for pristine cathodes, which can be considered as the mean frequency of cracks per unit area of the non-background phase. Thus, let $n_{\text{skelet}}^{(1)}, \ldots, n_{\text{skelet}}^{(m)} \geq 0$ be the number of cracks observed in the crack-wise segmentations $S_{\text{c}}^{(1)}, \ldots, S_{\text{c}}^{(m)}$, respectively. Then, the total number of cracks observed for pristine cathodes is given by $\sum_{i=1}^{m} n_{\text{skelet}}^{(i)}$. On the other hand, the total area $A > 0$ of the non-background phase observed in the $m = 9$ SEM images of pristine cathodes is given by

$$A = p^2 \sum_{i=1}^{m} \#\{x \in W \colon S^{(i)} > 0\}. \tag{11}$$

Then, the crack intensity λ is defined as the ratio

$$\lambda = \frac{\sum_{i=1}^{m} n_{\text{skelet}}^{(i)}}{A}. \tag{12}$$

Furthermore, we can compute structural descriptors for each individual crack $s \subset W$ observed in a crack-wise segmentation S_c. For example, the overall size of a crack $s \subset W$ can be described by its area-equivalent diameter $d > 0$ which is given by

$$d = 2p \sqrt{\frac{\#s}{\pi}}. \tag{13}$$

On the other hand, the length $\ell > 0$ of a crack $s \subset W$ can be characterized by the number of pixels associated with its corresponding curve L in the skeleton image C_{skelet} of S, i.e.,

$$\ell = p \cdot \#L. \tag{14}$$

Moreover, we characterize the width $b > 0$ of a crack $s \subset W$ by averaging the diameters of the largest inscribed circles in s centered at the pixels of its corresponding curve L. Therefore, we compute the Euclidean distance transform $D \colon W \to [0, \infty)$ of the crack phase in S given by

$$D(x) = \min\{\|x - y\| \colon y \in W, S(y) < 2\} \qquad \text{for each } x \in W. \tag{15}$$

Thus, for a pixel $x \in W$ associated with the crack phase (i.e., $S(x) = 2$) the value $D(x)$ is the distance of x to the non-crack phase. Consequently, the largest circle centered at x which is inscribed in the crack phase has a diameter of $2D(x)$ (in pixels). Thus, the width b of the crack s is given by

$$b = \frac{p}{\#L} \sum_{x \in L} 2D(x). \tag{16}$$

Finally, by computing the descriptor vector (d, ℓ, b) of crack size, length and width for each crack observed in the crack-wise segmentations $S_{\text{c}}^{(1)}, \ldots, S_{\text{c}}^{(m)}$ of pristine cathodes we obtain a dataset

$$\mathcal{X}_{\text{pristine}} = \Big((d_{\text{pristine}}^{(i)}, \ell_{\text{pristine}}^{(i)}, b_{\text{pristine}}^{(i)}) \Big)_{i=1}^{n_{\text{pristine}}}$$

of $n_{\text{pristine}} > 0$ crack descriptors. Note, however, that we disregard vectors (d, ℓ, b) for which the crack size d is smaller than $2.5p$, as the corresponding regions $s \subset W$ of the crack-wise segmentation may be caused by noise within the image data.

2.4.4 Analysis of crack growth during degradation

Analogously as described above, we compute the particle porosity $\rho_{i,j}$, the total area $A_{i,j}$ of the non-background phase, the crack intensity $\lambda_{i,j}$, and the dataset $\mathcal{X}_{i,j}$ of $n_{i,j}$ crack descriptors for each degradation scenario (i,j), where $i \in \{1\mathrm{C}, 6\mathrm{C}, 9\mathrm{C}\}, j \in \{25, 225, 600\}$.

Note that with increasing degradation of cathodes, cracks do not only grow, but also new (smaller) cracks are formed. Therefore, we present a method which limits the analysis of crack development during degradation as much as possible to crack growth, by disregarding small cracks. For example, for the crack intensities $\lambda_{\text{pristine}}$ and $\lambda_{6\mathrm{C},600}$ of pristine cathodes and the degradation scenario $(6\mathrm{C}, 600)$, respectively, we obtained that $\lambda_{\text{pristine}} = 0.145\,\mu\text{m}^{-2}$ and $\lambda_{6\mathrm{C},600} = 1.184\,\mu\text{m}^{-2}$. Thus, we assume that, in comparison to pristine cathodes, in the degraded cathodes of scenario $(6\mathrm{C}, 600)$ the difference $\lambda_{6\mathrm{C},600} - \lambda_{\text{pristine}} = 1.039\,\mu\text{m}^{-2}$ is attributed to the intensity of newly formed cracks. Crack growth of scenario $(6\mathrm{C}, 600)$ with respect to the pristine scenario can be examined by equalizing the intensities, i.e., by retaining from the dataset $\mathcal{X}_{6\mathrm{C},600}$ the $\widetilde{n}_{6\mathrm{C},600} = \lambda_{\text{pristine}} A_{6\mathrm{C},600}$ descriptor vectors which have the $\widetilde{n}_{6\mathrm{C},600}$ largest crack sizes d as an entry. We denote this adjusted dataset by $\widetilde{\mathcal{X}}_{6\mathrm{C},600}$. The cracks associated with this dataset are visualized in Figure 4. Analogously, by equalizing the intensities of the remaining degradation scenarios, we obtain the adjusted datasets $\widetilde{\mathcal{X}}_{i,j}$ for each degradation scenario (i,j) with $i \in \{1\mathrm{C}, 6\mathrm{C}, 9\mathrm{C}\}, j \in \{25, 225, 600\}$.

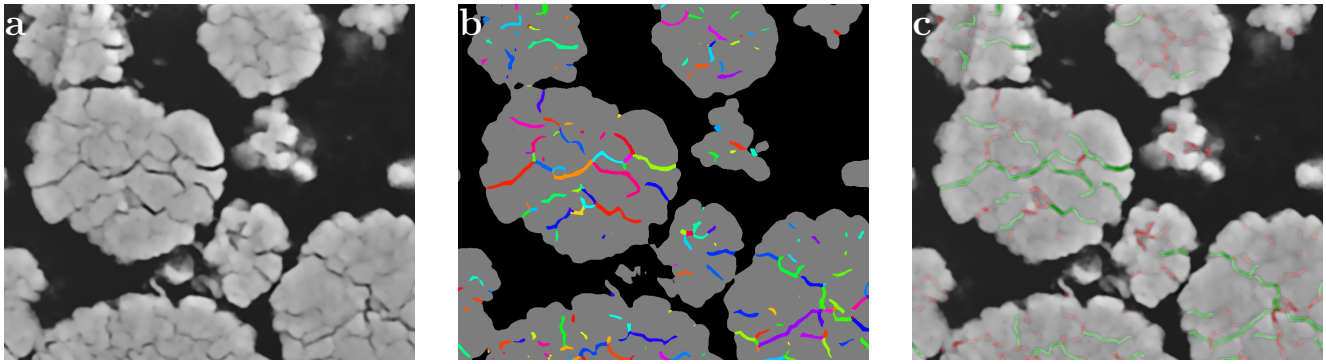

Figure 4: **Analysis of crack growth.** Cutout of a raw SEM image I (a) for the degradation scenario $(6\mathrm{C}, 600)$, and the crack-wise segmentation S_{c} (b). In (c) the cracks are overlayed in green and red color with the raw SEM image, where green color indicates cracks which have been retained in the adjusted dataset $\widetilde{\mathcal{X}}_{6\mathrm{C},600}$.

3 Results

In this section, we present some quantitative results of the structural analysis of cracks observed in SEM image data described in Section 2. More precisely, by applying the method given in Section 2.4.1, we obtain datasets T_{pristine} and $T_{(i,j)}$ of local thickness values for pristine cathodes and cycled cathodes for the degradation scenarios (i,j) with $i \in \{1\mathrm{C}, 6\mathrm{C}, 9\mathrm{C}\}, j \in \{25, 225, 600\}$, respectively. The corresponding mean values of these datasets are visualized in Figure 5a (blue lines). In order to characterize the distribution of the local thickness values, boxplots are shown in Figure 5b for the pristine and the degraded scenarios.

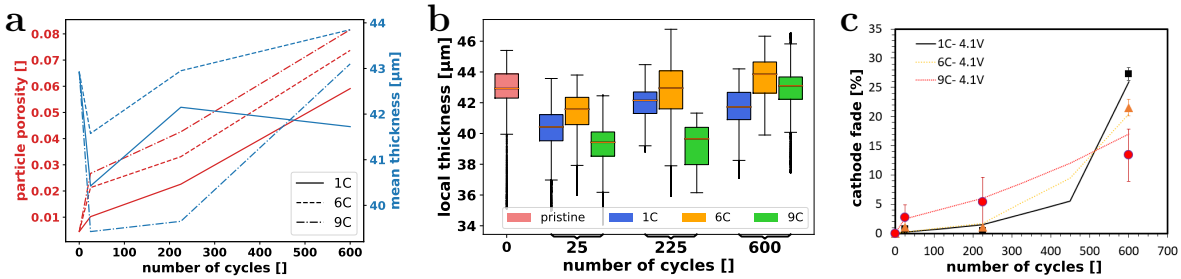

Figure 5: a: Influence of the number of recharge cycles on the particle porosity (red) and on the mean cathode thickness (blue). b: Boxplots of local thickness values computed from the datasets T_{pristine} and $T_{(i,j)}$ for each degradation scenario (i, j) with $i \in \{1\text{C}, 6\text{C}, 9\text{C}\}, j \in \{25, 225, 600\}$. c: Data replotted from Tanim et al. (2021)[21] showing the increase in loss of active material (LAM) on the NMC cathode as a function of Ah throughput for cells cycled between 2.8 V and 4.1 V at the specified C-rates.

Besides the local thickness values further descriptors have been considered in Section 2. For example, by means of Equation (10) we determine the particle porosity $\rho = 0.0045$ of pristine cathodes. The corresponding values for the particle porosities of degraded cathodes are given in Table 1 (left) and Figure 5a (red lines). For a visualization of the particle porosity as a function of the distance to the separator, see Supplementary Figure S1. The crack intensity λ of pristine cathodes is computed according to Equation (12), which leads to $\lambda = 0.145\,\mu\text{m}^{-2}$. The values obtained for the crack intensities of degraded cathodes are listed in Table 1 (right).

rate \cycles	25	225	600
1C	0.0102	0.0226	0.0591
6C	0.0213	0.0331	0.0737
9C	0.0267	0.0426	0.0816

rate \cycles	25	225	600
1C	0.29	0.521	1.06
6C	0.534	0.736	1.184
9C	0.607	0.859	1.239

Table 1: Left: Particle porosities of degraded cathodes, being larger than the particle porosity $\rho = 0.0045$ of pristine cathodes. Right: Crack intensities (in μm^{-2}) of degraded cathodes, being larger than the crack intensity $\lambda = 0.145\,\mu\text{m}^{-2}$ of pristine cathodes.

In order to characterize the distribution of crack size within pristine cathodes, Figure 6a (red box) visualizes the boxplot for the crack sizes $d^{(1)}_{\text{pristine}}, \ldots, d^{(n_{\text{pristine}})}_{\text{pristine}}$ within the dataset $\mathcal{X}_{\text{pristine}}$. Moreover, Figure 6a shows the corresponding boxplots of crack sizes for each degradation scenario (i, j) with $i \in \{1\text{C}, 6\text{C}, 9\text{C}\}, j \in \{25, 225, 600\}$, to visualize the influence of charge rate and the number of recharge cycles on the crack size distribution. Analogously, the corresponding boxplots of crack lengths and crack widths are shown in Figure 6b and c, respectively.

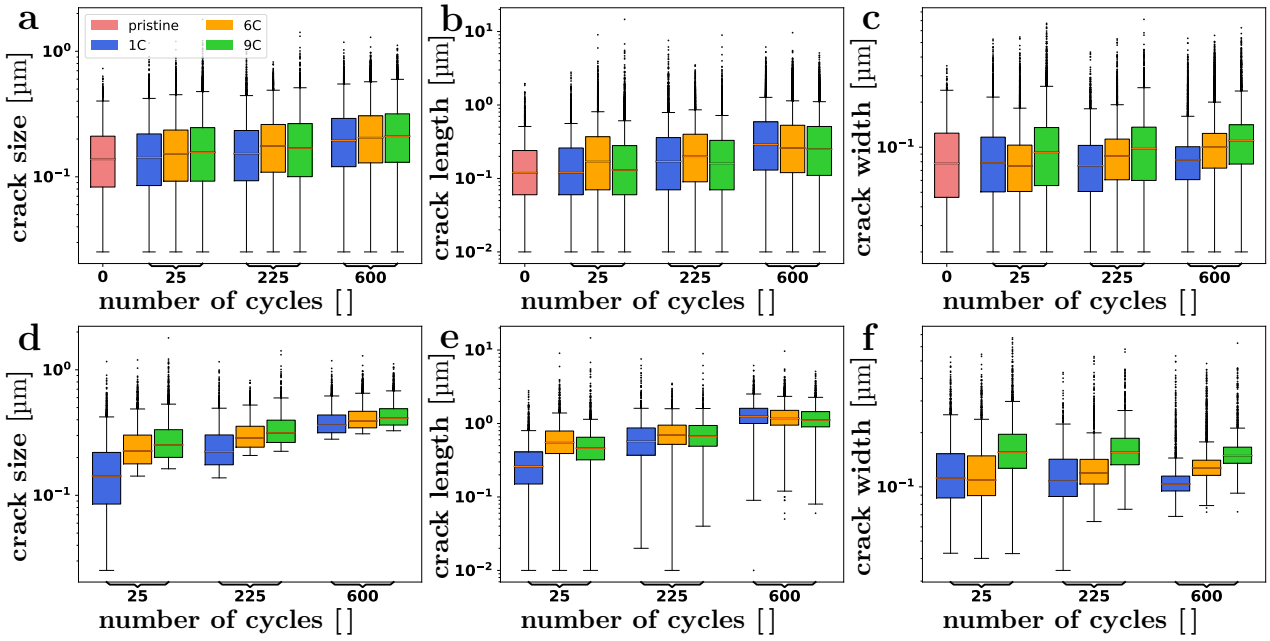

Figure 6: Top row: Boxplots of crack sizes (a), lengths (b) and width (c) computed from the datasets $\mathcal{X}_{\text{pristine}}$ and $\mathcal{X}_{i,j}$ for each degradation scenario (i,j) with $i \in \{1\text{C}, 6\text{C}, 9\text{C}\}, j \in \{25, 225, 600\}$. Bottom row: Boxplots of crack sizes (d), lengths (e) and width (f) computed from the adjusted datasets $\widetilde{\mathcal{X}}_{i,j}$ for each degradation scenario (i,j) with $i \in \{1\text{C}, 6\text{C}, 9\text{C}\}, j \in \{25, 225, 600\}$. The bottom and top ends of the boxes indicate the first and second quartiles. Median values are represented by red lines within the boxes. The whiskers show the 5th and 95th percentiles, whereas points indicate outliers.

Note that Figure 6a indicates that the C-rate might not have a significant influence on the crack size distribution. This could be explained by the fact that increasing degradation of cathodes does not only cause crack growth, but also leads to the formation of new (smaller) cracks, see Section 4 for further discussions. In order to investigate the influence of structural degradation on the crack growth, Figures 6d-f show the boxplots of crack descriptors which have been computed from the adjusted datasets $\widetilde{\mathcal{X}}_{i,j}$ introduced in Section 2.4.4, i.e., from the descriptor vectors consisting of the largest cracks for all $i \in \{1\text{C}, 6\text{C}, 9\text{C}\}, j \in \{25, 225, 600\}$.

The particle porosity in Figure 5a shows an increasing trend with cycle number. The increasing porosity of particles was hypothesized to cause the irreversible expansion of cells throughout their cycle life by increasing the porosity of electrodes and therefore the volume.[32] The thickness of the NMC electrodes were quantified from the SEM images, however as seen in Figure 5b the standard deviation of thicknesses measured was too large to confidently determine a trend. The particle porosity increases with the number of cycles and increases with C-rate where it is observed to have the most rapid change within the first 25 cycles during the "break-in" period. The "break-in" period is also observed in LAM in Figure 5c but the correlation with rate and cycles does not well match the particle porosity trend observed in Figure 5a.

4 Discussion

In Table 1 (left) and in Figure 5a we observe that both the number of cycles as well as the charge rate are positively correlated with the particle porosity. In particular, Figure 5a indicates that the charge rate has the greatest impact within the first 25 cycles. Afterwards, the number of cycles seems to be the driving force in the increase of particle porosity. Similarly, we observe that the cathode thickness increases with the number of cycles, see Figures 5a and b. However, for the pristine scenario the cathode thickness is relatively large, i.e., the mean thickness value is larger than most of the corresponding values for cycled cathodes. This could be attributed to local inhomogeneities in local cathode thicknesses and a general variability in thickness of 5–7 % for reverse comma coaters during manufacturing.[33]

The impact of the number of cycles on the structural degradation of cathode particles is also reflected in the size distribution of cracks. More precisely, Figures 6a-c indicate that the median values of crack size, length and width increase (almost) monotonously with the number of cycles. However, such monotonous effects are not generally observed for increasing charge rates. This phenomenon could be explained by the fact that the structural degradation of particles during cycling does not only lead to crack growth (i.e., a size, length and width increase of existing cracks) but also to the formation of new smaller cracks. In particular, the values of the crack intensities listed in Table 1 (right) indicate that the number of cracks grows with increasing charge rate and recharge cycle number. Thus, in order to investigate the crack growth behavior during cycling we determined the adjusted datasets $\widetilde{\mathcal{X}}_{i,j}$ for each degradation scenario (i, j) with $i \in \{1\text{C}, 6\text{C}, 9\text{C}\}, j \in \{25, 225, 600\}$ by disregarding small cracks. The corresponding boxplots of the crack sizes visualized in Figure 6d indicate that crack growth occurs with increasing charge rate and number of cycles. Moreover, we observe that cracks become longer with increasing number of cycles but, in general, not wider, see Figures 6e and f. On the other hand, with increasing C-rate, cracks become wider but generally not longer, see Figure 6e.

By correlating the results on the structural degradation of cathode particles with the electrochemical results depicted in Figure 5c, we observe that the influence of the charge rate onto the capacity fade seems to be inconclusive—indicating that particle porosity is not the dominant capacity fade mechanism. Moreover, the loss of active material is highest for low charge rates after 600 cycles, but particle porosities are approximately equal, indicating that cracks continue to play a minor role in capacity fade after high cycle numbers.

5 Conclusion

Crack evolution within NMC electrodes was quantified from SEM images by super resolving images and applying bespoke segmentation and feature quantification methods. This approach applies widely accessible and cost-effective capabilities that are demonstrated to quickly acquire data from hundreds of electrode particles that gave statistical confidence in the image-based measurements. Measuring crack evolution within NMC particles as a function of cycles and charge rate showed that cracks rapidly develop within the first 25 cycles and thereafter monotonically increase for the following hundreds of cycles with cracks primarily becoming longer rather than wider. Cracking was most severe for higher rates of charging where the rate dependence of cracking was most evident for the first 25 cycles. However, the capacity fade of the cell and the electrochemically measured loss of active material in the NMC electrode did not reflect the trend of cracking beyond the first 25 cycles, suggesting that while cracking may be the dominant factor for capacity fade early in the cell's cycle life, cracking is not the dominant degradation mode later in the cell's cycle life. While cracks may appear to correlate with capacity fade within cells, we show that they may not be the primary cause of capacity fade and that further materials research is needed to develop a causative understanding of degradation throughout the cells cycle life.

Data availability

The datasets generated during and/or analysed during the current study are available from the corresponding authors on reasonable request.

Code availability

All formulations and algorithms necessary to reproduce the results of this study are described in the Results and Methods sections.

Acknowledgements

This work was authored in part by the National Renewable Energy Laboratory, operated by Alliance for Sustainable Energy, LLC, for the U.S. Department of Energy (DOE) under Contract No. DE-AC36-08GO28308. Funding was provided by the U.S. DOE Office of Vehicle Technology Extreme Fast Charge Program, program manager Samuel Gillard. The views expressed in the article do not necessarily represent the views of the DOE or the U.S. Government. The U.S. Government retains and the publisher, by accepting the article for publication, acknowledges that the U.S. Government retains a nonexclusive, paid-up, irrevocable, worldwide license to publish or reproduce the published form of this work, or allow others to do so, for U.S. Government purposes. The authors acknowledge the support from Argonne National Laboratory, which is a U.S. DOE Office of Science Laboratory operated by UChicago Argonne, LLC, under Contract No. DE-AC02–06CH11357.

Author contributions

Elecrochemical data on cycled cathodes was acquired by T.R.T. SEM measurements were performed by Z.Y. Processing and statistical analysis of image data was performed by O.F. Main parts of the paper were written by D.P.F., O.F., T.R.T. and Z.Y. All authors discussed the results and contributed to writing of the manuscript. K.S. and V.S. designed and supervised the research.

Competing interests

The authors declare no competing financial or non-financial interests.

References

[1] Quinn, A., Moutinho, H., Usseglio-Viretta, F., Verma, A., Smith, K., Keyser, M., and Finegan, D. P. *Cell Rep. Phys. Sci.* **1**(8), 100137 (2020).

[2] Li, P., Zhao, Y., Shen, Y., and Bo, S.-H. *J. Phys.: Energy* **2**(2), 022002 (2020).

[3] Tsai, P.-C., Wen, B., Wolfman, M., Choe, M.-J., Pan, M. S., Su, L., Thornton, K., Cabana, J., and Chiang, Y.-M. *Energy Environ. Sci.* **11**, 860–871 (2018).

[4] Lin, F., Zhao, K., and Liu, Y. *ACS Energy Lett.* **6**(11), 4065–4070 (2021).

[5] Tian, C., Xu, Y., Nordlund, D., Lin, F., Liu, J., Sun, Z., Liu, Y., and Doeff, M. *Joule* **2**(3), 464–477 (2018).

[6] Finegan, D. P., Vamvakeros, A., Tan, C., Heenan, T. M., Daemi, S. R., Seitzman, N., Di Michiel, M., Jacques, S., Beale, A. M., Brett, D. J., Shearing, P. R., and Smith, K. *Nat. Commun.* **11**, 631 (2020).

[7] Ryu, H.-H., Park, K.-J., Yoon, C. S., and Sun, Y.-K. *Chem. Mater.* **30**(3), 1155–1163 (2018).

[8] Furat, O., Finegan, D. P., Diercks, D., Usseglio-Viretta, F., Smith, K., and Schmidt, V. *J. Power Sources* **483**, 229148 (2021).

[9] Furat, O., Petrich, J., Finegan, D. P., Diercks, D., Usseglio-Viretta, F., Smith, K., and Schmidt, V. *npj Comput. Mat.* **7**, 105 (2021).

[10] Allen, J., Weddle, P., Verma, A., Mallarapu, A., Usseglio-Viretta, F., Finegan, D., Colclasure, A., Mai, W., Schmidt, V., Furat, O., Diercks, D., Tanin, T., and Smith, K. *J. Power Sources* **512**, 230415 (2021).

[11] Lu, X., Zhang, X., Tan, C., Heenan, T. M. M., Lagnoni, M., O'Regan, K., Daemi, S., Bertei, A., Jones, H. G., Hinds, G., Park, J., Kendrick, E., Brett, D. J. L., and Shearing, P. R. *Energy Environ. Sci.* **14**, 5929–5946 (2021).

[12] Ryu, H.-H., Park, N.-Y., Seo, J. H., Yu, Y.-S., Sharma, M., Mücke, R., Kaghazchi, P., Yoon, C. S., and Sun, Y.-K. *Mater. Today* **36**, 73–82 (2020).

[13] Sun, G., Sui, T., Song, B., Zheng, H., Lu, L., and Korsunsky, A. M. *Extreme Mech. Lett.* **9**, 449–458 (2016).

[14] Park, N.-Y., Ryu, H.-H., Park, G.-T., Noh, T.-C., and Sun, Y.-K. *Adv. Energy Mater.* **11**(9), 2003767 (2021).

[15] Park, G.-T., Yoon, D. R., Kim, U.-H., Namkoong, B., Lee, J., Wang, M. M., Lee, A. C., Gu, X. W., Chueh, W. C., Yoon, C. S., and Sun, Y.-K. *Energy Environ. Sci.* **14**, 6616–6626 (2021).

[16] Heenan, T. M. M., Wade, A., Tan, C., Parker, J. E., Matras, D., Leach, A. S., Robinson, J. B., Llewellyn, A., Dimitrijevic, A., Jervis, R., Quinn, P. D., Brett, D. J. L., and Shearing, P. R. *Adv. Energy Mater.* **10**, 2002655 (2020).

[17] Xia, S., Mu, L., Xu, Z., Wang, J., Wei, C., Liu, L., Pianetta, P., Zhao, K., Yu, X., Lin, F., and Liu, Y. *Nano Energy* **53**, 753–762 (2018).

[18] Petrich, L., Westhoff, D., Feinauer, J., Finegan, D. P., Daemi, S. R., Shearing, P. R., and Schmidt, V. *Comput. Mater. Sci.* **136**, 297–305 (2017).

[19] Furat, O., Finegan, D. P., Diercks, D., Kirstein, T., Smith, K., and Schmidt, V. *npj Comput. Mater.* **8**, 68 (2022).

[20] Ledig, C., Theis, L., Huszár, F., Caballero, J., Cunningham, A., Acosta, A., Aitken, A., Tejani, A., Totz, J., Wang, Z., and Shi, W. In *Proceedings of the IEEE Conference on Computer Vision and Pattern Recognition*, 105–114 (IEEE Computer Society, Honolulu, HI, USA, 2017).

[21] Tanim, T. R., Yang, Z., Colclasure, A. M., Chinnam, P. R., Gasper, P., Lin, Y., Yu, L., Weddle, P. J., Wen, J., Dufek, E. J., Bloom, I., Smith, K., Dickerson, C. C., Evans, M. C., Tsai, Y., Dunlop, A. R., Trask, S. E., Polzin, B. J., and Jansen, A. N. *Energy Storage Mater.* **41**, 656–666 (2021).

[22] Ronneberger, O., Fischer, P., and Brox, T. In *Proceedings of Medical Image Computing and Computer-Assisted Intervention,* Navab, N., Hornegger, J., Wells, W. M., and Frangi, A. F., editors, 234–241 (Springer, Cham, Switzerland, 2015).

[23] Abadi, M., Agarwal, A., Barham, P., Brevdo, E., Chen, Z., Citro, C., Corrado, G. S., Davis, A., Dean, J., Devin, M., Ghemawat, S., Goodfellow, I., Harp, A., Irving, G., Isard, M., Jia, Y., Jozefowicz, R., Kaiser, L., Kudlur, M., Levenberg, J., Mané, D., Monga, R., Moore, S., Murray, D., Olah, C., Schuster, M., Shlens, J., Steiner, B., Sutskever, I., Talwar, K., Tucker, P., Vanhoucke, V., Vasudevan, V., Viégas, F., Vinyals, O., Warden, P., Wattenberg, M., Wicke, M., Yu, Y., and Zheng, X. (2015). Software available from tensorflow.org.

[24] Bertoldo, J. P., Decencière, E., Ryckelynck, D., and Proudhon, H. *Front. Mater.* **8**, 493 (2021).

[25] Ho, Y. and Wookey, S. *IEEE Access* **8**, 4806–4813 (2019).

[26] Phan, T. H. and Yamamoto, K. Preprint at `https://arxiv.org/abs/2006.01413`, (2020).

[27] Kingma, D. P. and Ba, J. In *Proceedings of the 3rd International Conference on Learning Representations,* Bengio, Y. and LeCun, Y., editors (ICLR, San Diego, CA, USA, 2015).

[28] Goodfellow, I., Bengio, Y., and Courville, A. *Deep Learning.* MIT Press, (2016).

[29] Lee, T., Kashyap, R., and Chu, C. *CVGIP Graph. Models Image Proc.* **56**(6), 462–478 (1994).

[30] Chinga, G. and Helle, T. *Nord. Pulp Pap. Res. J.* **17**(3), 307–312 (2002).

[31] Neumann, M., Charry, E. M., Zojer, K., and Schmidt, V. *Methodol. Comput. Appl. Probab.* **23**, 613–627 (2021).

[32] Bond, T., Gauthier, R., Eldesoky, A., Harlow, J., and Dahn, J. R. *J. Electrochem. Soc.* **169**(2), 020501 feb (2022).

[33] Zwierlein, S. Presented at International Battery Seminar & Exhibit, (2022).